Hydrogen Separation of Methyltriethoxysilane Templating Silica Membrane

Jong-Ho Moon and Chang-Ha Lee
Dept. of Chemical Engineering, Yonsei University, Seoul 120-749, Korea

DOI 10.1002/aic.11344
Published online October 23, 2007 in Wiley InterScience (www.interscience.wiley.com).

Hydrogen separation on microporous methyltriethoxysilane-templating silica composite/α-alumina membranes (below MTES membrane) was studied using three binary gas mixtures: H_2/N_2, H_2/CO_2, and H_2/CH_4. The characteristics of unsteady and steady-state permeation/separation on the MTES membrane were compared to each other. Although permeation flux in the H_2/N_2 mixture was comparatively low, H_2 selectivity was high (H_2/N_2 SF $\approx$ 30–60). On the contrary, the H_2/CO_2 mixture showed high permeation flux but low H_2 selectivity (H_2/CO_2 SF $\approx$ 1.5–6.5). The H_2/CH_4 mixture showed a large difference between permselectivity (28–48) and separation factor (10–22). Results from this study revealed that it was difficult to predict the separation factor using the one-component permeation ratio (permselectivity) over the experimental range tested. These separation characteristics could be primarily ascribed to the molecular size and structure of each gas, which likely contributed to steric hindrance or molecular sieving within the membrane pore. In addition, the adsorption affinity of each molecule on the membrane surface acted as a key factor in separation performance because it significantly influenced surface diffusion. The generalized Maxwell-Stefan model incorporating the dust gas model, and the Langmuir model could successfully predict the transient and steady-state permeation/separation. *AIChE J,* 53: 3125–3136, 2007
Keywords: MTES templating, silica membrane, hydrogen separation, surface diffusion, molecular sieving

Introduction

The steady depletion of fossil fuel reserves makes hydrogen-based energy sources increasingly attractive. Therefore, hydrogen production and separation technologies have received enormous attention in the industrial and academic fields.[1,2] The competitiveness of membrane systems for gas separation is predicted to be relatively equivalent to other methods for small and intermediate scale applications. Membrane systems are also likely to offer increased flexibility of operation, thus membranes are likely to eventually challenge the present commercial status of cryogenics and pressure swing adsorption.[3] Furthermore, microporous inorganic membranes offer excellent thermal and chemical stability, good erosion resistance, and high-pressure stability relative to conventional polymeric membranes. Microporous ceramic membranes with surface diffusion and molecular sieve properties have both relatively high gas permeance and good selectivity at higher temperatures. In addition, they are likely to be used in membrane reactors for conversion enhancement in dehydrogenation and methane reforming reactions during hydrogen production.[4,5]

In the synthesis of hydrogen-permselective amorphous silica-based membranes, sol–gel processing has received the most attention due to its excellent processibility and its potential to precisely control pore size and structure.[6–8] In addition,

Correspondence concerning this article should be addressed to Chang-Ha Lee at leech@yonsei.ac.kr.

organic template-derived amorphous/nanoporous silica composite membranes with uniform pore sizes comparable to those in silica or zeolite membranes have been getting attention. These membranes offer a high separation factor and high permeances stemming from molecular sieving.[9–11]

Recently, it was reported that zeolite or CMS membranes showed excellent separation factor for H_2/CH_4 mixture compared with other H_2/CO_2 and H_2/N_2 mixtures.[12–15] Generally, the gas-separation mechanisms for zeolite and CMS are equilibrium and kinetic control, respectively. On the other hand, it was reported that an METS-templating silica membrane showed the characteristics of both equilibrium and kinetic control for these molecules because of the relatively mild adsorption affinity and pore size of thin-templating silica layer.[10–11] Because H_2 mixture from off-gas or reforming gas consists of multicomponent, the separation mechanism of various binary H_2 mixtures should be elucidated at first. Furthermore, understanding equilibrium and kinetic separations in inorganic membranes is important to develop an efficient membrane system. In the case of adsorptive and molecular-sieving materials, such as zeolite or CMS (carbon molecular sieve) membranes, many researchers have already studied permeation/separation mechanisms in extensive detail.[16–26] However, in contrast to these membranes, modeling and simulation studies using organic-templating silica membranes have been very limited.[11]

In this study, the separation of three binary H_2 mixtures in an MTES-templating silica membrane was investigated as a function of pressure and temperature. H_2/N_2, H_2/CO_2, and H_2/CH_4 were investigated to elucidate the role of molecular size, adsorption affinity, and molecular structure in membrane separation. To depict the theoretical permeation and separation mechanisms, this study adopted the GMS (generalized Maxwell-Stefan) model that incorporated the DGM (dust gas model) and the Langmuir model adapted to material balance. The permeation flux and selectivity were evaluated using steady-state permeation of binary mixtures. The transport behavior of each mixture was also analyzed using unsteady-state permeation and separation experiments.

Theory

Transport of gases through inorganic membranes is influenced by various mechanisms, including Knudsen diffusion, viscous diffusion, and surface diffusion. Moreover, the surface diffusion through a membrane is related to other factor such as the adsorption equilibrium of strongly adsorbed components.[3]

A quantitative description of mass transfer in porous media must ensure the local conservation of mass for each participating species. In this study, a dynamic model incorporating mass and energy balances was adopted to analyze the permeation mechanism.

Transient permeation

The mass balance of a component, i, in an infinitesimal volume can be presented as follows[10,19]:

$$\frac{\varepsilon}{RT}\frac{\partial P_i}{\partial t}+(1-\varepsilon)\frac{\partial q_i}{\partial t}=-\frac{1}{r}\frac{\partial\left(rN_i^{\mathrm{tot}}\right)}{\partial r}\quad(i=1,\cdots,n)\qquad(1)$$

where P_i is the partial pressure, q_i is the adsorbed phase concentration, ε is the porosity, and N_i^{tot} is the overall molar flux.

Equation 1 states that the local partial pressure and concentration of the adsorbed species change with time, depending on the transport rate of the components. The total permeation flux is composed of pore diffusion and surface diffusion:

$$N_i^{\mathrm{tot}}=\left(\frac{\varepsilon}{\tau}\right)N_i^{\mathrm{P}}+(1-\varepsilon)N_i^{\mathrm{S}}\qquad(2)$$

where N_i^{P} is the flux by pore diffusion, N_i^{S} is the flux by surface diffusion, and τ is the tortuosity factor.

Pore diffusion (DGM)

At the experimental pressure range, it was assumed that the collisions between a molecule and the pore wall occur more frequently than intermolecular collisions and there is a difference in total pressure between the ends of a capillary. Therefore, the molecular diffusion was neglected in the separation mechanism. The macro- or mesopore diffusion can be expressed as follows:

$$N_i^{\mathrm{P}}=N_i^{\mathrm{Kn}}+N_i^{\mathrm{Vis}}\qquad(3)$$

where N_i^{Kn} is the Knudsen diffusion and N_i^{Vis} is the viscous diffusion.

The multicomponent pore diffusion consisting of Knudsen diffusion and Poiseuille diffusion can be expressed by the DGM (Dusty gas model).[3,10,19]

$$N_i^{\mathrm{P}}=-\frac{\varepsilon}{\tau}\frac{1}{RT}\left(D_i^{\mathrm{Kn}}+\frac{B_i^0}{\eta_i}P_i\right)\frac{\partial P_i}{\partial r}\qquad(4)$$

For a homogeneous porous structure, the pore diffusion contains the two parameters, D_i^{Kn} (Knudsen diffusivity: Eq. 5) and B_i^0 (viscous diffusion parameter: Eq. 6). These can be determined by the following equations[27]:

$$D_i^{\mathrm{Kn}}=\frac{2r_{\mathrm{P}}}{3}\sqrt{\frac{8RT}{\pi M_i}}\qquad(5)$$

$$B_i^0=\frac{r_{\mathrm{P}}^2}{8}\qquad(6)$$

where r_{P} is the pore radius, R is the ideal gas constant, T is temperature, M is molecular weight, η_i is the viscosity of each gas, τ is the tortuosity of the membrane layer, D_i^{Kn} is Knudsen diffusivity, B_i^0 is viscous diffusion constant, and η_i is viscosity of component i.[20,21]

Surface diffusion (GMS)

There was significant adsorption on the pore wall, especially in the MTES-templating silica layer.[11] The diffusion through the adsorbed phase (surface diffusion) was considered in the model.

The molar flux by the surface diffusion can be calculated by the GMS model combined with the surface coverage. The GMS model is based on the assumption that the movement of species is caused by a driving force balanced by the friction of the moving species.[16] The diffusion of adsorbed species is derived by taking the gradient of the thermodynamic

potential as the driving force and treating vacancies as participating species:

$$-\frac{\theta_i}{RT}\nabla\mu_i = \sum_{\substack{j=1\\ j\neq i}}^{n}\frac{\theta_j N_i^S - \theta_i N_j^S}{q^{sat}\rho D_{ij}} + \frac{N_i^S}{q^{sat}\rho D_i}, \quad (i,j=1,2,\cdots,n) \tag{7}$$

The first term on the right-hand side represents the friction due to the counter exchange of adsorbed molecules, while the second term represents surface friction.

In this study, the Maxwell-Stefan diffusivity, $Đ_i^S$, and the surface coverage, θ_i, in Eq. 7 were calculated by the following Langmuir isotherm model (Eq. 8):

$$\theta_i = \frac{q_i}{q_i^{sat}} = \frac{b_i P_i}{1+\sum_{j=1}^{n} b_j P_j} \tag{8}$$

where q_i^{sat} is the saturated amount of adsorption and b_i is Langmuir parameter of component i.

The chemical potential gradient can be related to the gradient in the surface coverage by a matrix of thermodynamic factor.[20–23]

$$\frac{\theta_i}{RT}\nabla\mu_i = \sum_{j=1}^{n}\Gamma_{ij}\nabla\theta_i \tag{9}$$

The thermodynamic potential gradient, $\bigtriangledown\mu_i$, can be expressed in terms of the gradients of the surface occupancies by the matrix of thermodynamic factors given by:

$$\Gamma_{ij} = \theta_i\frac{\partial \ln P_i}{\partial\theta_j} \quad (\text{for one component; } i=j) \tag{10}$$

The surface fluxes through a membrane in a single (Eq. 11) and a binary (Eq. 12) system are derived by the combination of Eqs. 8–10:

$$N_1^S = -\rho(1-\varepsilon)q_1^{sat}\frac{Đ_1^S}{1-\theta_1}\nabla\theta_1 \quad (i=1,2,\ldots,n) \tag{11}$$

$$N_1^S = -\rho(1-\varepsilon)q_1^{sat}\frac{Đ_1^S}{1-\theta_1-\theta_2} \times \frac{\left[(1-\theta_2)+\theta_1\frac{Đ_2^S}{Đ_{12}^S}\right]\nabla\theta_1 + \left[\theta_1+\theta_1\frac{Đ_2^S}{Đ_{12}^S}\right]\nabla\theta_2}{\theta_2\frac{Đ_1^S}{Đ_{12}^S}+\theta_1\frac{Đ_2^S}{Đ_{12}^S}+1} \tag{12}$$

In some special cases, the friction between molecules is much less important than the friction within the wall. In these cases, $Đ_{ij}^S$ $(=\infty)$ is much larger than $Đ_i^S$, and Eq. 12 can be reduced to

$$N_1^S = -\rho(1-\varepsilon)q_1^{sat}\frac{Đ_1^S}{1-\theta_1-\theta_2}[(1-\theta_2)\nabla\theta_1+\theta_1\nabla\theta_2] \tag{13}$$

If molecule–molecule interactions cannot be ignored, Eq. 12 can be used. $Đ_{ij}^S$ from the single-component diffusivities (Eq. 14) can be determined by using the empirical relation[20,24]:

$$Đ_{ij}^S = Đ_i^{S\,\theta_i/(\theta_i+\theta_j)}\,Đ_i^{S\,\theta_j/(\theta_i+\theta_j)} \tag{14}$$

The cross-term diffusivities satisfy the Onsager reciprocity relation[20,23]

$$Đ_{ij}^S = Đ_{ji}^S \tag{15}$$

Heat effect

The overall energy balance can be expressed as follows[25,26]:

$$\Delta H_{ads}\,A\left(N_{i,in}^{tot}-N_{i,out}^{tot}\right) = \rho C_p V\frac{\partial T}{\partial t} + h_i A(T_{in}-T_{out}) \tag{16}$$

where ΔH_{ads} is the heat of adsorption on the membrane, A is the effective membrane area, C_p is the heat capacity, V is the volume of the layer, h_i is the convective heat transfer coefficient of the feed gas, and T_{out} is the feed temperature.

The change of temperature leads to variation of surface diffusivity and adsorption equilibrium. The temperature dependency of surface diffusivity can be expressed by the following Arrhenius-type relationship[27]:

$$Đ_i = Đ_{0,i}\exp\left(\frac{-E_D}{RT}\right) \tag{17}$$

where E_D is the diffusional activation energy and $Đ_{0,i}$ is the diffusivity at infinite temperature. The temperature dependency of adsorption parameters, q_i^{sat} and b_i, can be calculated with the LRC (loading ratio correlation) using the Langmuir isotherm,[28] and b_i is related to heat of adsorption using the van't Hoff equation[22]:

$$q_i^{sat} = k_1/T^{k_2} \tag{18}$$

$$b_i = b_{i,0}\exp\left(\frac{\Delta H_{ads}}{RT}\right) \tag{19}$$

where k_1 and k_2 are the fitting parameters and $b_{i,0}$ is the Langmuir parameter at zero loading.

Models

This study applied the following four models to the experimental results to evaluate the importance of equations mentioned earlier:

Model 1: Permeation flux predicted from single gas data and permselectivity calculated from partial feed pressures.

Model 2: Prediction of multicomponent permeation from single gas diffusion model using Darken-type diffusivity (Eq. 11).

Model 3: Prediction of multicomponent permeation from GMS model without intermolecular diffusion ($Đ_{ij}=\infty$, Eq. 12).

Model 4: Prediction of multicomponent permeation from GMS model with intermolecular diffusion ($Đ_{ij}\neq\infty$, Eq. 13).

Experimental

Membrane preparation

A MTES sol as the structure-directing agent was used for the templating material in the fabrication of a nanoporous silica/α-alumina composite membrane. The $SiO_2/\alpha\text{-}Al_2O_3$ composite support (1.6-nm mean pore diameter) was prepared using a pressurized coating of colloidal silica sol inside tubular $\alpha\text{-}Al_2O_3$ supports (7.8-mm outside diameter, 6.2-mm inside diameter, 0.8-mm thickness, 100-mm length, and 0.1-μm mean pore diameter). In this study, a MTES sol was used as the templating material in the fabrication of a nanoporous silica/α-alumina composite membrane. This organic material could serve as a suitable template in the formation of a "zeolitelike" armophous silica membrane with a uniform pore radius of ~3 Å.[8,9] The organic-templating silica sol was prepared from the mixture of silica sol and organic template MTES (99% purity, Aldrich, USA), and the organic-templating silica composite membrane was fabricated by dip coating the $SiO_2/\alpha\text{-}Al_2O_3$ composite supports in the templating silica sols. The whole process of dip coating, drying, and calcining was repeated 12 times to repair any defects in the silica layer. The pore size of the silica composite membrane was controlled using TEOS-EtOH solution. The details of the membrane synthesis and characteristics have been previously described.[8,9]

Permeation experiments

In the study, the permeation experiments in the inorganic membrane were performed at temperatures between 323 and 473 K and at a pressure between 100 and 700 kPa. All gasses used for permeation and separation experiments had greater than 99.99% purity. The three binary mixtures selected for this study were H_2/N_2, H_2/CO_2, and H_2/CH_4 (50:50 v/v). The permeation experiment for each condition was performed up to three times, and the results shown were within less than ±3% deviation at each condition.

The permeation of pure gases was measured in dead-end mode without the retentate stream, while permeation/separation of binary mixtures was measured in stage-cut mode controlling feed and retentate flow rates. The permeation flux and separated composition were measured using a mass flow meter and online quadrupole mass spectrometer (QMG 422, Balzers, Germany). Experiments investigating the depressurization (DP, feed pressure → atmospheric pressure) step and the pressurization (PR, atmospheric pressure → feed pressure) step were performed to elucidate the permeation/separation mechanism.

Experiments were performed using a tubular-type membrane with an ID of 6.2 mm and an effective length of 8.6 cm. The effective permeation area of the membrane was 16.89 cm^2. The membrane was placed in a stainless steel tubular module. The cell consisted of a sweeping gas inlet line and a three-way permeated outlet line to prevent the stagnation of permeated gases. The inlet gas line, inner cell, and outer cell were equipped with thermocouples (RTD type, Pt 100 Ω) to measure the system temperature. A thermocouple was placed in the center of the cell to measure the inner cell temperature. Pressure was measured by two pressure transducers located at the inlet and the permeate of the cell. Feed gas was controlled by an MFC (mass flow controller) and a gas cylinder pressure regulator. Retentate gas was controlled by another MFC and a BPR (back-pressure regulator). The flow rate of the permeated gas was measured by an MFM (mass flow meter), a soap bubble flow meter, or a wet gas meter. Before the experiments, the membrane cell was activated at 250°C and placed under vacuum conditions to remove the residual adsorbed gas species. Detailed descriptions of the experimental system and the permeation measurement procedure can be found in a previous study.[10,11]

Numerical simulation

In this study, the gPROMS modeling tool (Process Systems Enterprise) was used to obtain the solution of dynamic simulation from the mathematical model mentioned above. A centered finite difference method of the second order was applied to the spatial partial derivatives. The differential-algebraic equations for the temporal domain were subsequently integrated by employing an integrator, called DASOLV, included in the gPROMS library. The results of numerical simulation were stable for the range of conditions used in this study.

Results and Discussion

Single gas permeation

In the previous study,[11] single gas permeation fluxes of H_2, CH_4, N_2, and CO_2 were measured under dead end condition. In this study, the separation mechanisms of the membrane are assumed to be determined solely by the silica layer because of its large adsorption capacity and small pores in comparison with the α-alumina support. As shown in Figure 1, the validity of the assumption was confirmed since the simulated results using the combined DGM (Eq. 4) and GMS models (Eq. 11) agreed well with the experimental data.[10,11]

Figure 1a reveals that H_2 showed an almost linear permeation flux that was proportional to feed pressure at a fixed temperature of 373 K. In contrast, the permeation fluxes of CO_2, N_2, and CH_4 were nonlinearly proportional to feed pressure. Moreover, CO_2 permeation exhibited particularly strong favorable curvature and comparatively high flux, which were ascribed to its high adsorption affinity and structure.[7] The steady-state permeation fluxes of N_2 and CH_4 were much lower than those of H_2 and CO_2.

It is noteworthy that the temperature dependency of CO_2 at the feed pressure of 500 kPa is different from the others, as shown in Figure 1b. The permeate fluxes of H_2, CH_4, and N_2, increased with temperature. On the other hand, the permeate flux of CO_2 was highest at low temperature (323 K), but decreased with increasing temperature. Because the levels of adsorption and affinity generally increase in a manner inversely proportional to temperature, the low temperature will contribute to the surface diffusion of CO_2 in the membrane. However, the permeation fluxes of H_2, CH_4, and N_2 molecules increased with temperature due to increased mobility of the molecules in the MTES membrane pores.[2,10,11] Moreover, the effect of temperature on the permeate flux of H_2 was significant due to its molecular size and low adsorption affinity relative to the other molecules.

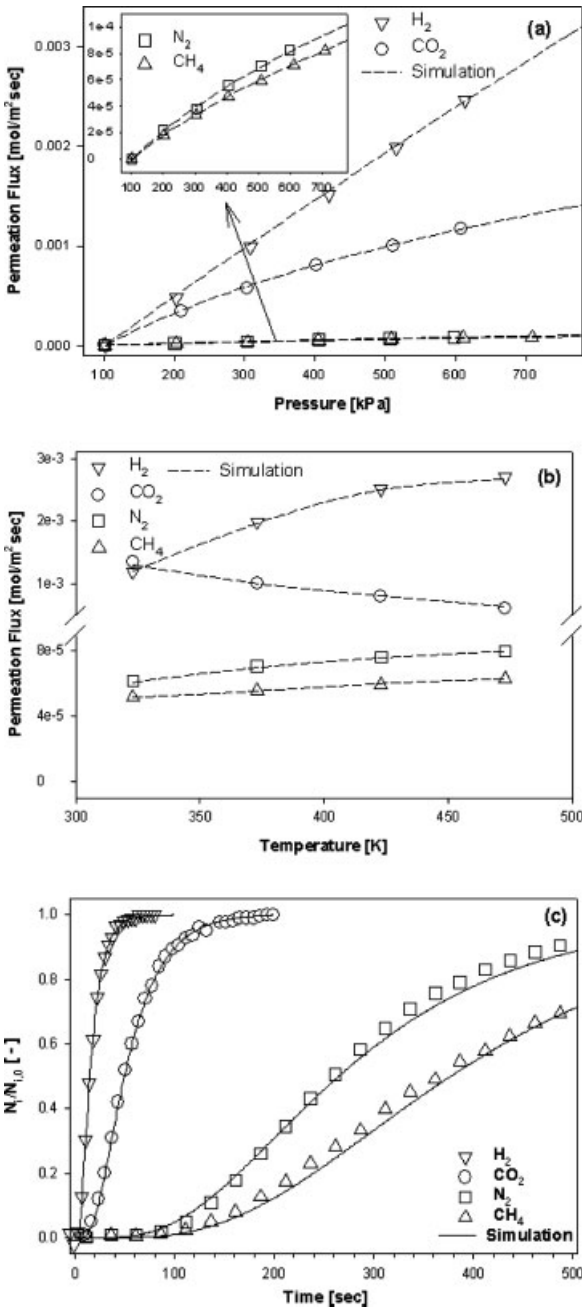

Figure 1. Experimental and simulated permeation fluxes of H_2, CO_2, CH_4, and N_2 on MTES-templating silica/α-alumina composite membrane under dead end (stage cut = 1) condition.[10,11]

(a) Pressure effect at 373 K, (b) temperature effect, and (c) single gas transient permeation.

As shown in Figure 1c, H_2 reached steady state within approximately 30 s, significantly earlier than the other molecules. CO_2 reached steady state at about 200 s, while N_2 and CH_4 took longer than 1000 s to reach steady state. The permeation flux and rate of CO_2, with its linear structure and relatively small kinetic diameter (3.30 Å), were much higher and faster than those of CH_4 or N_2. This was due to the strong adsorption affinity and capacity. H_2 had the smallest kinetic diameter (2.92 Å) and the weakest adsorption affinity. This molecule showed the highest and fastest permeation flux. On the contrary, the permeation rate of CH_4 was the slowest of all the molecules studied despite its high adsorption affinity. This was due to steric hindrance or molecular sieving attributed to its tetrahedral structure and relatively large kinetic diameter (3.82 Å). Even though N_2 has a linear structure, the permeation rate was low due to its large kinetic diameter (3.64 Å).[11]

In general, the ideal permselectivity of gas-separation membranes is used as an indicator of quality. In this study, the ideal permselectivities of the H_2 binary systems were calculated from the single gas permeability using the following equation, and the results are presented in Table 1.

$$\alpha_{AB}^{perm} = N_A^{tot}/N_B^{tot} \qquad \text{(at the same operating condition)} \quad (20)$$

As seen in Table 1, higher selectivity can be obtained at higher temperatures from the perspective of permselectivity. In addition, the H_2/CH_4 system shows the highest selectivity compared to the other H_2 mixtures.

In the binary system, the separation factor, α_{AB}, can be calculated by following equation instead of Eq. 20:

$$\alpha_{AB} = \frac{y_A/y_B}{x_A/x_B} = \frac{y_A/(1-y_A)}{x_A/(1-x_A)} \quad (21)$$

where x and y are the feed and permeation composition, respectively, and component A is the more permeable molecule.

The actual selectivities (Eq. 21, separation factor) of binary mixtures differed from the actual selectivities calculated from single gas permeation results presented in Figure 1b. This result implies that it is difficult to predict the selectivity of gas mixture accurately using measurements from single gas experiments. The details will be discussed in the next section with experimental and simulated results of binary mixtures.

Binary mixture permeation

Permeation fluxes of the binary mixtures, H_2/N_2, H_2/CO_2, and H_2/CH_4 (50:50 v/v), were measured as functions of pressure and temperature while other conditions, such as feed flow rate, stage cut, and sweeping gas flow rate, were held constant. Figures 2, 4, and 6 show steady-state permeation fluxes and separation factors of H_2/N_2, H_2/CO_2, and H_2/CH_4

Table 1. The Permselectivity of H_2/N_2, H_2/CO_2 and H_2/CH_4 by Using Single Gas Permeation Fluxes at 500-kPa Feed Pressure (400 kPa Pressure Drop) and 323–473 K Temperature Range

	Permselectiviy (−)		
	H_2/N_2	H_2/CO_2	H_2/CH_4
323 K	19.30	0.88	23.01
373 K	28.09	1.99	35.76
423 K	32.89	3.12	42.25
473 K	33.85	4.45	42.85

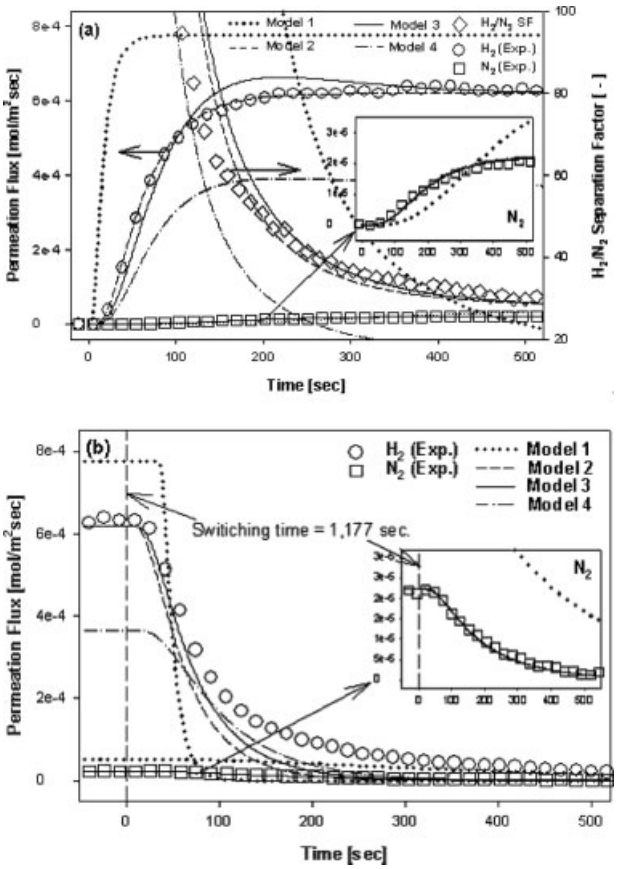

Figure 2. Transient permeation flux of H_2/N_2 binary mixture (50/50 v/v) on MTES membrane at 323.15 K and 600 kPa.

(a) PR (pressurization) step and (b) DP (depressurization) step. Other operating conditions, such as sweeping gas flow rate (=50 sccm) and stage cut (=0.60), were held constant. Symbols are experimental data and lines are simulation results.

binary mixtures on the MTES membrane, respectively. Figures 3, 5, and 7 present transient permeation curves at the corresponding H_2 mixture.

The permeability of the three H_2 binary systems at 323–473 K is presented in Table 2. The average permeability was calculated through the steady-state flux of binary gas mixture. The permeability of the H_2 binary mixture in the membrane was 1.30–2.82 $\times$ 10^{-9} mol m^{-2} s^{-1} Pa^{-1}, and the sequence of the average permeability was $H_2/CO_2 > H_2/N_2 > H_2/CH_4$.

In this study, the Maxwell-Stefan diffusivities obtained from single gas permeation were re-estimated by fitting the experimental results of binary gas permeation. The parameters obtained from the experimental data at the pressurization (PR) step were applied to the results of the depressurization (DP) step. In addition, the parameters estimated at specific temperature, and pressure conditions (such as Figure 2) were applied to predict the steady-state permeation and separation factors measured under different experimental conditions (such as Figure 3). For comparison, the diffusivities obtained from single (Model 1) and binary gas permeation (Models 2–4) are presented in Table 3.

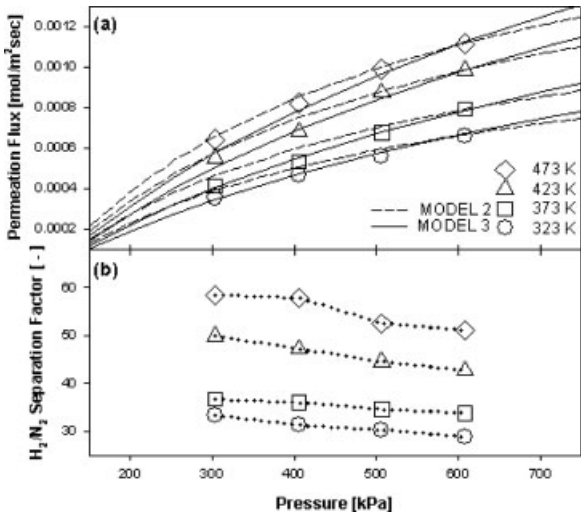

Figure 3. Steady-state permeation of H_2/N_2 binary mixture (50/50 v/v) on MTES membrane at 323.15–473.15 K.

(a) Permeation flux and (b) H_2/N_2 separation factor. Other operating conditions, such as sweeping gas flow rate (=50 sccm) and stage cut (=0.60), were held constant. Symbols are experimental data and lines are simulation results.

H_2/N_2 mixture

Figure 2 shows the transient permeation curves, (a) PR and (b) DP, of the H_2/N_2 mixture at 373 K and 600 kPa (500 kPa pressure drop). The permeation flux of H_2 reached plateau at about 250 s during the PR step. H_2 molecules with small kinetic diameters (2.92 Å) then began to permeate within 10 s. In contrast, the permeation of N_2, which has a comparatively large kinetic diameter (3.64 Å), was observed at 90 s and reached plateau within 500 s. This result was significantly different from the results of single gas permeation presented in Figure 1c. This is because H_2 single gas reached plateau within about 30 s, and N_2 single gas took over 1000 s to reach steady state. In the H_2/N_2 binary mixture, the permeation rate of N_2 increased and that of H_2 decreased compared to single gas permeation. This implies that N_2 permeation is enhanced by H_2 permeation, while H_2 permeation rate is inhibited by the slow permeation rate of N_2.

Figure 2b demonstrates that the transient permeation of H_2 showed some different behaviors at the DP and PR steps. In contrast, the transient curve of N_2 at the DP step agreed with the transient behavior at the PR step. The permeation flux of H_2 during 100 s of the DP step decreased drastically, which corresponded to the steep increase of permeation flux during

Table 2. The Average Permeablitiy of H_2/N_2, H_2/CO_2, and H_2/CH_4 Binary Mixtures Calculated from the Experimental Results at 100–600 kPa and 323–473 K

	Permeability (mol m^{-2} s^{-1} Pa^{-1})		
	H_2/N_2 ($\times 10^{-9}$)	H_2/CO_2 ($\times 10^{-9}$)	H_2/CH_4 ($\times 10^{-9}$)
323 K	1.40	1.84	1.30
373 K	1.66	2.54	1.68
423 K	2.11	2.78	1.96
473 K	2.43	2.85	2.36

Table 3. Darken-Type Diffusivity from Previous Study[11] (Model 1) and Maxwell-Stefan Diffusivity [Model 2 (Eq. 11), 3 (Eq. 13), and 4 (Eq. 14)]

		$\mathcal{D}_i$ (m^2/s)			
		H_2 ($\times 10^{-11}$)	N_2 ($\times 10^{-12}$)	CO_2 ($\times 10^{-11}$)	CH_4 ($\times 10^{-12}$)
Model 1	Single gas	*8.50	*2.55	*1.69	*1.27
Model 2	H_2/N_2	1.70	4.10	–	–
	H_2/CO_2	2.20	–	1.38	–
	H_2/CH_4	1.90	–	–	3.50
Model 3 and 4	H_2/N_2	1.70	4.10	–	–
	H_2/CO_2	2.20	–	1.38	–
	H_2/CH_4	1.90	–	–	3.50

*Referred from Moon et al.[11]

the same period in the PR step, as presented in Figure 2a. However, a tailing phenomenon was observed during the DP step after 100 s, and the permeation flux did not reach steady state until 450 s. This implies that small H_2 molecules with low adsorption affinity remain in the pore near atmospheric pressure condition.

Figure 2 compares the experimental data and simulated results calculated from the various aforementioned models. Model 1, which uses the results of single gas permeation, shows large deviation from the experimental data. As can be seen in Figure 2a, the transient and steady-state permeation fluxes predicted by Model 1 were much faster and higher than those of the experimental data. As a result, the permeation flux at the DP step was higher and the tailing could not be predicted. On the contrary, the simulated permeation rate of N_2 was slower at the early period, but the crossover was observed after passing a certain period of time in Figure 2a. Because the permeation flux at steady state became larger than the experimental data at the PR step, the simulated result at the DP step naturally showed a large deviation. This implies that diffusion parameters obtained from single gas permeation do not accurately predict multicomponent permeation.

The roll-up phenomenon is caused by the displacement of a weaker adsorbate by a stronger one in the adsorption process.[2,29] The permeation flux of weak adsorbate with a small molecular size steeply increased with time. On the other hand, the permeation flux of the strong adsorbate with a large molecular size is small due to the adsorption in the pores for a certain period of time. However, if the adsorption of the strong adsorbate reaches its saturated amount, the permeation flux of the weak adsorbate decreases owing to the increased permeation flux of the strong adsorbate. The roll-up phenomenon can also be observed in the case when the strong adsorbate has faster permeation flux because of the hindrance effect of the weak adsorbate in the pore.[30]

In Model 2 (Eq. 11), the single gas diffusion model using the Darken-type diffusivity was extended to binary gas permeation. The extended Langmuir model (Eq. 5) that incorporates competitive adsorption was used as the isotherm model. Model 2 was also developed based on single gas permeation; therefore, the roll-up phenomenon[2,29] cannot be described, but Model 3 (Eq. 13, $\mathcal{D}_{ij} = \infty$, ignoring intermolecular diffusion) and 4 (Eq. 12, $\mathcal{D}_{ij} \neq \infty$, considering intermolecular diffusion) can describe it. As shown in Figure 2a, the roll-up phenomenon was not observed in this study because of the thin membrane layer and a weak adsorption of H_2. In the permeation flux of H_2 at the PR step, the prediction by Model 2 was more accurate than that by the other models in Figure 2a. In addition, Model 3 could predict the permeation flux reasonably, but the deviation was larger than that of Model 2 due to the roll up of the permeation flux prediction. In the case of the permeation flux of H_2 at the DP step, Model 3 was slightly better than Model 2 in Figure 2b, but the other models showed a large deviation. However, the permeation flux of N_2 could be predicted accurately by Models 2–4 at both PR and DP steps. Therefore, in this study, Models 2 and 3 were applied to the prediction of the other binary systems including the steady state and unsteady-state permeation fluxes.

Figure 3 shows the steady-state permeation curve and separation factor of the H_2/N_2 mixture at 323–473 K temperature range. The average H_2/N_2 binary mixture permeability was 1.40–2.43 $\times$ 10^{-9} mol m^{-2} s^{-1} Pa^{-1}, and the H_2/N_2 separation factor was 28.85–51.05. Because of increased mobility of the molecules in the MTES membrane pores, the permeation fluxes of H_2/N_2 binary mixture increased with an increase in temperature in Figure 3a. The separation factor of H_2/N_2 binary mixture increased with temperature at a fixed pressure, but it decreased with an increase in pressure at fixed temperature in Figure 3b. The permeability of the MTES membrane was much lower than that of CMS membrane (1.5 $\times$ 10^{-6} mol m^{-2} s^{-1} Pa^{-1} at 298 K), but the separation factor was slight better than CMS membrane (30–40 at 298–423 K).[14] And, its permeability was comparable to that of zeolite membrane (8.3 $\times$ 10^{-9} mol m^{-2} s^{-1} Pa^{-1} at 523 K).[12] On the other hand, its permeability was higher than that of polymeric membrane (1.8 $\times$ 10^{-10} mol m^{-2} s^{-1} Pa^{-1} at 308 K),[31] while the separation factor was lower (50–70 at 298–323 K).[32]

Because both H_2 and N_2 molecules have weak adsorption affinity on the membrane, the permeation mechanism of the H_2/N_2 binary mixture is dominated by molecular sieving or pore diffusion rather than by surface diffusion caused by adsorption. Because N_2 molecules are not strongly adsorbed on the pore walls, the permeation of H_2 molecules is not disturbed by the improved mobility of N_2 molecules. In addition, it was reported that the permeation flux of pure H_2 gas was more affected by a change of temperature than that of pure N_2 gas.[11] However, because increased pressure contributes to overcoming the steric hindrance of N_2 molecules, H_2/N_2 separation factor decreased with increasing pressure at a

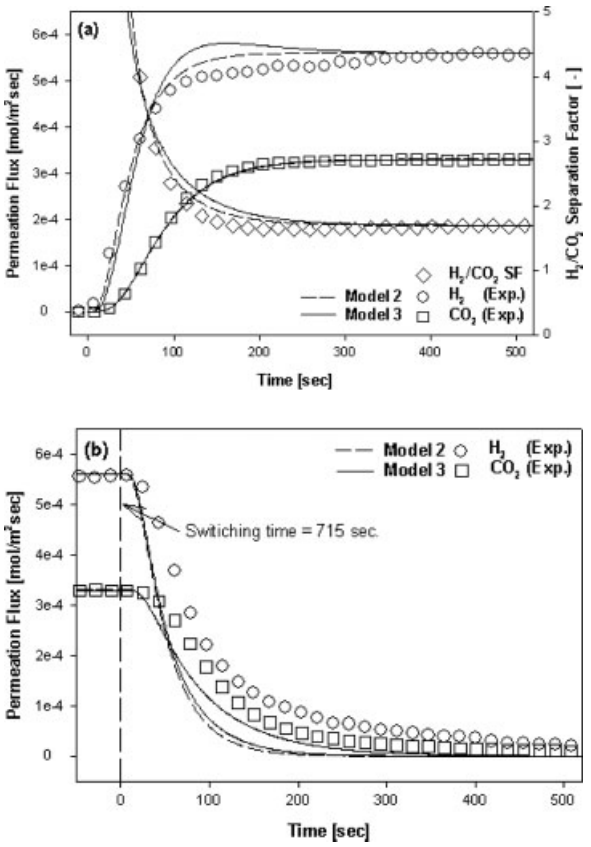

Figure 4. Transient permeation flux of H_2/CO_2 binary mixture (50/50 v/v) on MTES membrane at 323.15 K and 600 kPa.

(a) PR (pressurization) step and (b) DP (depressurization) step. Other operating conditions, such as sweeping gas flow rate (=50 sccm) and stage cut (=0.60), were held constant. Symbols are experimental data and lines are simulation results.

fixed temperature. In the H_2/N_2 binary mixture consisting of two weakly adsorbing gases, the separation factors approached the permselectivity while the permeation flux became smaller than the results of single gas permeation.

H_2/CO_2 mixture

Figure 4 shows the transient permeation curves [(a) PR and (b) DP] for the H_2/CO_2 mixture at 373 K and 600 kPa (500 kPa pressure drop). The simulated results of H_2 transient permeation in H_2/CO_2 binary mixtures predicted by Model 2 was more accurate at the PR step, while Model 3 was more accurate at the DP step. However, in the case of CO_2 permeation, both Models 2 and 3 were well fitted to the experimental data and showed similar values.

Both H_2 and CO_2 molecules began to permeate within 10 s during the PR step. The permeation flux of H_2 was close to reaching its plateau (steady state) by ~150 s and subsequently underwent a steady increase until 300 s. On the other hand, the permeation flux of CO_2 reached its steady state within 250 s. In the case of this mixture, combined differences in diffusivity and adsorption affinity might be a driving force of permeation. Because the competitive adsorption and pore filling of components occur in the silica layer of the membrane, little permeation is observed at the beginning of the PR step. After a certain period of time, weakly adsorbed H_2 begins to permeate through the membrane pore. However, as the adsorption proceeds, the vacant sites in the pore become occupied by CO_2, and the surface concentration of CO_2 is intensified. This leads to the hindrance of the H_2 permeation due to the pore blockage by CO_2. In addition, because of their weak adsorption affinity and small/linear structure, H_2 molecules permeated more easily and rapidly than CO_2. Similar to the above H_2/N_2 binary mixture, compared to the single gas permeation in Figure 1c, the permeation rate of CO_2 became faster but that of H_2 became slower in H_2/CO_2 binary mixture. CO_2 permeation is assumed to be enhanced by H_2 permeation; however, the H_2 permeation rate is disturbed by CO_2 in the pore.

Unlike for the DP step in H_2/N_2 transient permeation in Figure 2b, the permeation flux of H_2 at the DP step in Figure 4b was considerably delayed (longer tailing). H_2 permeation was also expected to be hindered by the strongly adsorbed CO_2 molecules. Because H_2 permeation is affected by pore diffusion rather than surface diffusion, diminished pressure drop during the DP step cannot play an important role as driving force.[11] On the contrary, in the case of CO_2 permeation, the deviance between the times to reach the steady state in the PR and DP steps is relatively small. As reported in our previous studies,[10,11] surface diffusion is the dominant transport mechanism of CO_2 on the MTES membrane. Because concentration of strongly adsorbed CO_2 is maintained for a certain period on MTES membrane, it can be a driving force for CO_2 flux during the DP step.

As shown in Figures 5a, b, the steady-state permeation flux and the separation factor in the H_2/CO_2 system increased with the increase in the feed pressure. The average permeability was 1.84–2.85 $\times$ 10^{-9} mol m^{-2} s^{-1} Pa^{-1}, and the separation factor was 1.68–6.45. The separation factor of the MTES membrane was lower than that of the other types of membrane (3.9–6.8 at 373–474 K for zeolite membrane,[13] 10.7 at 523 K for CMS membrane,[15] 8–8.5 at 293–303 K for polymeric membrane[33]). However, its permeability was higher than that of CMS membrane (3.2 $\times$ 10^{-10} mol m^{-2} s^{-1} Pa^{-1} at 523 K)[15] and polymeric membrane (8.2 $\times$ 10^{-17} mol m^{-2} s^{-1} Pa^{-1} at 593 K)[34] except for that of zeolite membrane (5 $\times$ 10^{-7} mol m^{-2} s^{-1} Pa^{-1} at 473 K).[13]

The permeation flux of the H_2/CO_2 mixture was higher than the other binary systems, such as H_2/N_2 and H_2/CH_4. This was due to the strong surface diffusion effect and comparatively small kinetic diameter (3.30 Å) of CO_2. However, H_2 selectivity was lower with H_2/CO_2 than with other binary gas mixtures. In the case of the H_2/CO_2 mixture, surface diffusion and molecular sieving occurred simultaneously; thus, the flux of H_2 was significantly hindered by the CO_2 occupying the pores. Therefore, the increase in selectivity resulting from the increase in pressure shown in Figure 5b was almost negligible compared to the results of the H_2/CO_2 system shown in Figure 3b. However, as temperature increased, the permeation fluxes of H_2 increased steeply while those of CO_2 decreased. Namely, pore occupation of CO_2 by adsorption force was diminished drastically by increasing temperature, but the molecular mobility of H_2 was increased. There-

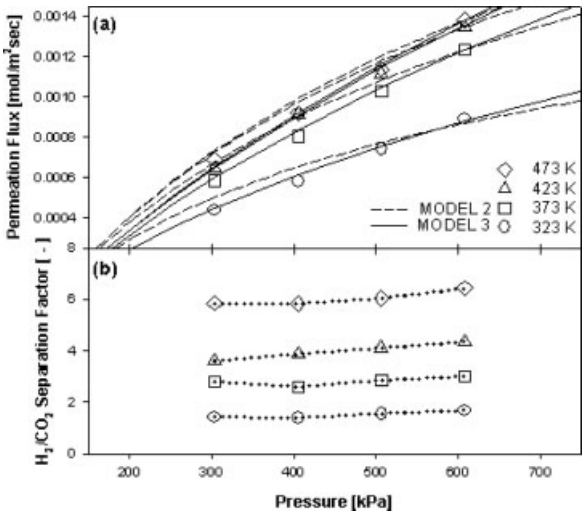

Figure 5. Steady-state permeation of H_2/CO_2 binary mixture (50/50 v/v) on MTES membrane at 323.15–473.15 K.

(a) Permeation flux and (b) H_2/CO_2 separation factor. Other operating conditions, such as sweeping gas flow rate (=50 sccm) and stage cut (=0.60), were held constant. Symbols are experimental data and lines are simulation results.

fore, the higher separation factor was observed at the higher temperature.

H_2/CH_4 mixture

Figure 6a shows the transient permeation curves of the H_2/CH_4 mixture at 373 K and 600 kPa during the PR step. The permeation flux of H_2 reached plateau at about 200 s; however, but the permeation flux for CH_4 took over 1100 s to reach steady state. In the case of the single gas permeation experiments in MTES membrane (Figure 1c), the permeation rate of CH_4 was much slower than that of H_2. In addition, the permeation rate of CH_4 in the H_2/CH_4 system became faster than that of the single gas permeation. On the contrary, the permeation rate of H_2 was decreased considerably compared to the results using single gases. Figure 6b shows the transient permeation of H_2/CH_4 mixture during the DP step. Similar to the behavior of the H_2/N_2 system, the H_2 permeation flux at the beginning of the DP step decreased drastically and a tailing phenomenon was observed after 100 s. CH_4 has a strong adsorption affinity, comparatively large kinetic diameter, and tetrahedral structure. Therefore, this molecule blocked the pore channels and somewhat disturbed H_2 permeation. In addition, the permeation rate of CH_4 during the PR and DP steps was still much slower than that of N_2 and CO_2 due to the steric hindrance.

The simulated results for CH_4 in the H_2/CH_4 system predicted by Models 2 and 3 fit the experimental data well. In the case of H_2, Model 2 using Darken-type diffusivity showed better agreement than Model 3 using Maxwell-Stefan diffusivity. The simulated result obtained from Model 3 showed a weak roll-up phenomenon for H_2, owing to competitive adsorption with CH_4. However, roll-up phenomena were not observed in the experiment because of low adsorption within the thin membrane layer.

As shown in Figure 7, the average permeability for the H_2/CH_4 system was 1.30–2.36 $\times$ 10^{-9} mol m^{-2} s^{-1} Pa^{-1}, and the separation factor was 10.49–20.74. The separation factor of the MTES membrane was high, but it was still much lower than that of zeolite membrane (533–321 at 373–474 K)[13] and CMS membrane (<200 at 523 K).[15] In addition, the permeability of zeolite membrane was also much higher than that of the MTES membrane (2 $\times$ 10^{-6} mol m^{-2} s^{-1} Pa^{-1} at 473 K).[13]

The prediction by Model 2 fit the experimental data better than the prediction by Model 3. The permeated flux and the separation factor in the H_2/CH_4 system increased simultaneously with an increase in feed pressure or temperature. This was also observed with the H_2/CO_4 system. However, the separation factor of the H_2/CH_4 system at 373–473 K was affected by the feed pressure more than the separation factor of the H_2/CO_4 system. This result implies that the improvement of H_2 permeation flux by increasing pressure is higher than that of CH_4 due to the steric hindrance and decreased

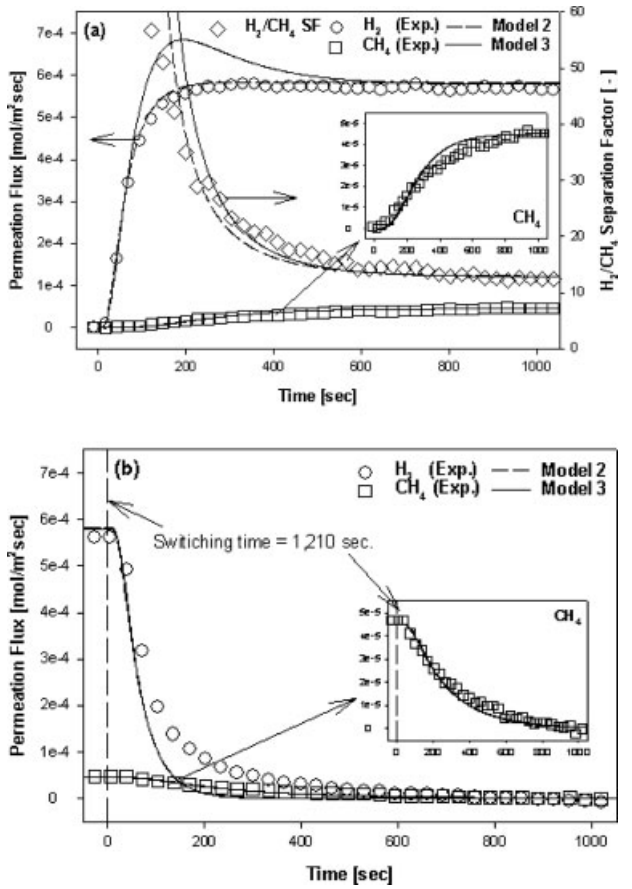

Figure 6. Transient permeation flux of H_2/CH_4 binary mixture (50/50 v/v) on MTES membrane at 323.15 K and 600 kPa.

(a) PR (pressurization) step and (b) DP (depressurization) step. Other operating conditions, such as sweeping gas flow rate (=50 sccm) and stage cut (=0.60), were held constant. Symbols are experimental data and lines are simulation results.

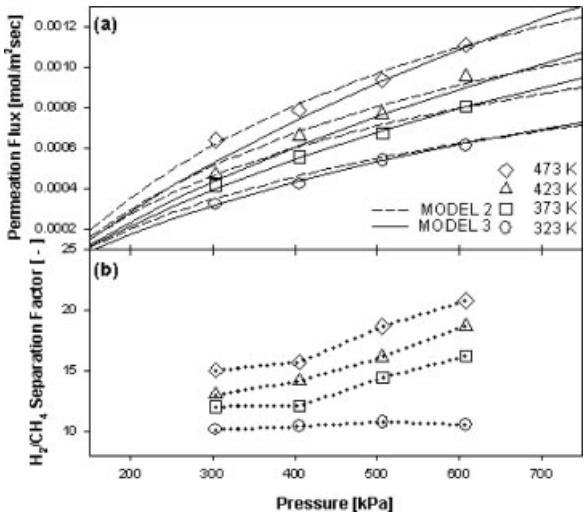

Figure 7. Steady-state permeation of H_2/CH_4 binary mixture (50/50 v/v) on MTES membrane at 323.15–473.15 K.

(a) Permeation flux and (b) H_2/CH_4 separation factor. Other operating conditions, such as sweeping gas flow rate (=50 sccm) and stage cut (=0.60), were held constant. Symbols are experimental data and lines are simulation results.

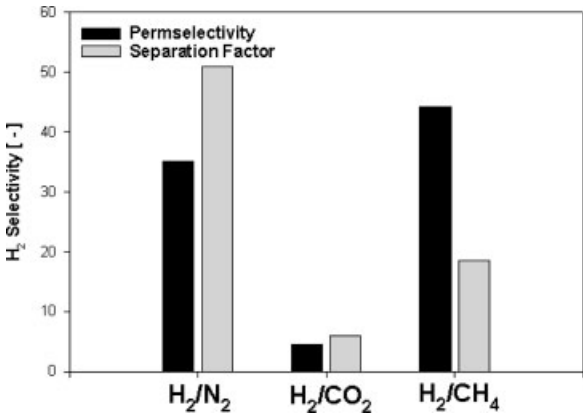

Figure 8. Comparison between permselectivities and separation factors of H_2 binary mixtures at 373 K and 500 kPa (400 kPa pressure drop).

adsorption amount of CH_4. At low temperature, the increased adsorption amount of CH_4 with pressure might prevent H_2 molecules from permeation.

Hydrogen separation

Table 4 shows the separation factor of the H_2/N_2, H_2/CO_2, and H_2/CH_4 systems at 500 kPa (400 kPa pressure drop) and 323–473 K temperature range. The sequence of the separation factor is $H_2/N_2 > H_2/CH_4 > H_2/CO_2$ under the same conditions.

Figure 8 shows comparison between permselectivity and separation factor of H_2 binary mixtures at 373 K and 500 kPa (400 kPa pressure drop). As shown in Figure 8, the separation factors for the H_2/N_2 and the H_2/CO_2 systems showed higher values than the permselectivities obtained from single gas permeation experiments (Table 1). On the other hand, the separation factor of the H_2/CH_4 system was lower than permselectivity. This is because H_2 permeation is prevented by the structural hindrance and strong adsorption affinity of CH_4.

It is also noteworthy that the separation factor of the H_2/CH_4 system is smaller than that of the H_2/N_2 system, even though the permselectivity of the H_2/CH_4 system is slightly higher than that of the H_2/N_2 system. However, the difference between permselectivity and separation factor was small in the H_2/CO_2 system.

As a result, when the permeation mechanism is dominated by adsorption equilibrium, the permselectivity is similar to the separation factor. On the other hand, when the permeation mechanism is controlled by adsorption equilibrium as well as kinetics, the permselectivity is different from the separation factor because the permeation flux in the MTES membrane is affected by the surface diffusion originated by adsorption property as well as molecular sieving. In this case, the kinetic parameters should be obtained from the mixture for accurate prediction.

Table 4. The Separation Factor of H_2/N_2, H_2/CO_2, and H_2/CH_4 Systems at 500 kPa with 400 kPa Pressure Drop and 323–473 K Temperature Range kPa Feed Pressure

	Separation Factor (−)		
	H_2/N_2	H_2/CO_2	H_2/CH_4
323 K	28.85	1.68	10.49
373 K	33.81	3.00	16.17
423 K	42.68	4.36	18.64
473 K	51.05	6.45	20.74

Conclusions

The permeation/separation characteristics for H_2 binary mixtures, H_2/N_2, H_2/CO_2, and H_2/CH_4 (50:50 v/v), were studied using MTES silica/alumina membranes. In the case of the H_2/N_2 and the H_2/CH_4 mixtures, although the permeation fluxes of the MTES membrane are comparatively low (permeabilities of $H_2/N_2 \approx 1.40$–2.43×10^{-9} mol m^{-2} s^{-1} Pa^{-1}, $H_2/CH_4 \approx 1.30$–2.36×10^{-9} mol m^{-2} s^{-1} Pa^{-1}), results demonstrated high H_2 selectivities (H_2/N_2 SF $\approx$ 30–60; H_2/CH_4 SF $\approx$ 10–22). In contrast, the separation factor for the H_2/CO_2 mixture was low (H_2/CO_2 SF $\approx$ 1.5–6.5) and had high permeability (1.84–2.85 $\times 10^{-9}$ mol m^{-2} s^{-1} Pa^{-1}).

For mixtures of H_2 and comparatively large molecules, such as N_2 and CH_4, the permselectivity of H_2/CH_4 was slightly higher than that of the H_2/N_2 system. However, the separation factor of the H_2/CH_4 system was smaller than that of the H_2/N_2 system. For mixtures of H_2 and molecules with strong adsorption affinity, such as CO_2 and CH_4, the separation factor of the H_2/CO_2 system was far smaller than that of the H_2/CH_4 system. However, the difference in separation factor between these two systems was much smaller than the difference in permselectivity. In addition, the H_2/CH_4 system reached steady state much slower than the H_2/N_2 system due to the structural hindrance and molecular sieving effect of

CH_4. The separation factor was increased with temperature in all the systems, while the effect of pressure on the separation factor differed. The separation factor of the H_2/CH_4 system was increased with pressure while that of the H_2/N_2 system was decreased. In addition, the change of separation factor by pressure was negligible in the H_2/CO_2 system.

When the adsorption equilibrium is a dominant permeation mechanism, such as in the H_2/CO_2 system, the permselectivity is similar to the separation factor. On the other hand, when the permeation mechanism is dominated by adsorption equilibrium and kinetics, the permselectivity is different from the separation factor (such as the H_2/N_2 and H_2/CH_4 systems). The permeation flux in the MTES membrane is presumed to be affected by the surface diffusion as well as molecular sieving. Therefore, the kinetic parameters, such as diffusivities, should be estimated from the mixture behaviors for more accurate prediction. In this study, the experimental results of unsteady-state permeation agreed well with the mathematical model using surface diffusion (Darken type equation and generalized Maxwell-Stefan model) and micropore diffusion (dusty gas model).

Acknowledgments

We gratefully acknowledge the Seoul R&BD Program for their financial support and the fostering project of the Specialized Graduate School of Hydrogen & Fuel Cell by MOCIE for graduate student support.

Notation

b_i = parameter in the Langmuir isotherm model (Pa^{-1})
$b_{0,i}$ = parameter of species i in the Langmuir isotherm model at zero loading (Pa^{-1})
B_i^0 = Poiseuille structural parameters of species i (m^2)
D_i^{Kn} = Knudsen diffusivity of species i ($m^2\ s^{-1}$)
$\mathcal{D}_{0,i}$ = Maxwell-Stefan surface diffusivity at infinite temperature ($m^2\ s^{-1}$)
$\mathcal{D}_i^S$ = Maxwell-Stefan surface diffusivity ($m^2\ s^{-1}$)
E_a = activation energy ($J\ mol^{-1}$)
ΔH_{ads} = heat of adsorption ($J\ mol^{-1}$)
k_1 = temperature dependant parameter for saturated adsorption capacity (mol/g)
k_2 = temperature dependant parameter for saturated adsorption capacity (−)
M_i = molecular weight of species i ($mol\ g^{-1}$)
N_i = molar flux of species i ($mol\ m^{-2}\ s^{-1}$)
N_i^{Kn} = molar flux of Knudsen diffusion of species i ($mol\ m^{-2}\ s^{-1}$)
N_i^P = molar flux of pore diffusion of species i ($mol\ m^{-2}\ s^{-1}$)
N_i^S = molar flux of surface diffusion of species i ($mol\ m^{-2}\ s^{-1}$)
N_i^{tot} = total molar flux of species of i ($mol\ m^{-2}\ s^{-1}$)
N_i^{Vis} = molar flux of viscous diffusion of species i ($mol\ m^{-2}\ s^{-1}$)
P_i = partial pressure of species i (Pa)
q_i = adsorbed species concentration within layer pores ($mol\ g^{-1}$)
q_i^{sat} = saturated capacity of adsorbed species i ($mol\ g^{-1}$)
R = gas constant, 8.314 ($J\ mol^{-1}\ K^{-1}$)
r_P = pore radius (m)
T = absolute temperature (K)
t = time (s)
x_i = feed composition of component i
y_i = permeation composition of component i

Greek letters

Γ_{ij} = thermodynamic factor of species i,j
ε = porosity of membrane
η_i = viscosity of species i (Pa s)
θ_i = fractional surface occupancy of species i
μ_i = chemical potential of species i ($J\ mol^{-1}$)
ρ = membrane density ($g\ m^{-3}$)
τ = tortuosity factor

Subscripts/superscripts

$i,j,1,2$ = component $i,j,1,2$
vis = viscous flow
Kn = Knudsen flow
tot = total flow
sat = saturated

Literature Cited

1. Kim MB, Ahn HW, Lee CH. Comparison of adsorption dynamics in kinetic and equilibrium beds in hydrogen ternary system. *Sep Sci Technol*. 2004;39:2951–2976.
2. Lee CH, Yang JY, Ahn HW. Effects of carbon-to-zeolite ratio in layered bed PSA for H_2 recovery from coke oven gas. *AIChE J*. 1999;45:535–549.
3. Burggraaf AJ, Cot L. *Fundamentals of Inorganic Membrane Science and Technology*. Amsterdam: Elsevier, 1996:331–433.
4. Asaeda M, Yamasaki S. Separation of inorganic/organic gas mixtures by porous silica membranes. *Sep Purif Technol*. 2001;25: 151–159.
5. Seo BK, Watanabe M, Kusakabe K, Morooka S, Kim SS. Formation of hydrogen permselective silica membrane for elevated temperature hydrogen recovery from a mixture containing steam. *Gas Sep Purif*. 1996;10:187–195.
6. Raman NK, Brinker CJ. Organic "template" approach to molecular sieving silica membranes. *J Membr Sci*. 1995;105:273–279.
7. Xomeritakis G, Naik S, Braunbarth CM, Cornelius CJ, Pardey R, Brinker CJ. Organic-templated silica membrane. I. Gas and vapor transport properties. *J Membr Sci*. 2003;215:225–233.
8. Yang SM, Lee YE, Hyun SH, Lee CH. Organic-templating approach to synthesis of nanoporous silica composite membranes. I. TPA-templating and CO_2 separation. *J Mater Sci*. 2002;37:2519–2525.
9. Lee YE, Kang BS, Hyun SH, Lee CH. Organic-templating approach to synthesis of nanoporous silica composite membranes. II. MTES-templating and CO_2 separation. *Sep Sci Technol*. 2004;39:3541–3557.
10. Moon JH, Park YJ, Kim MB, Hyun SH, Lee CH. Permeation and separation of a carbon dioxide/nitrogen mixture in a methyltriethoxysilane templating silica/α-alumina composite membrane. *J Membr Sci*. 2005;250:195–205.
11. Moon JH, Bae YS, Hyun SH, Lee CH. Equilibrium and kinetic characteristics of five single gases in a methyltriethoxysilane templating silica/α-alumina composite membrane. *J Membr Sci*. 2006;285:343–352.
12. Caro J, Noack M, Kolsch P, Schafer R. Zeolite membranes—state of their development and perspective. *Micro Meso Mater*. 2000;38:3–24.
13. Renate MV, Henk V. High-selectivity, high-flux silica membranes for gas separation. *Science*. 1998;279:1710–1711.
14. Wang LJ, Franklin CNH. Effects of surface treatments and annealing on carbon-based molecular sieve membranes for gas separation. *Appl Surf Sci*. 2005;240:161–174.
15. Aadesh H, Hwang HT, Paul KTL, Muhammad S, Theodore TT. Experimental studies of a hybrid adsorbent-membrane reactor (HAMR) system for hydrogen production. *Chem Eng Sci*. 2007;62:4126–4137.
16. Keizer K, Uhlhorn RJR, van Vuren RJ, Burggraaf AJ. Gas separation mechanisms in microporous modified γ-Al_2O_3 membranes. *J Membr Sci*. 1988;39:285–300.
17. Vroon ZAEP, Keizer K, Gilde MJ, Verweij H, Burggraaf AJ. Transport properties of alkanes through ceramic thin zeolite MFI membranes. *J Membr Sci*. 1996;113:293–300.
18. Chen YD, Yang RT. Preparation of carbon molecular sieve membrane and diffusion of binary mixtures in the membrane. *Ind Eng Chem Res*. 1994;33:3146–3153.
19. Tuchlenski A, Uchytil P, Seidel-Morgenstern A. An experimental study of combined gas phase and surface diffusion in porous glass. *J Membr Sci*. 1998;140:165–184.

20. Krishna R. Multicomponent surface diffusion of adsorbed species: a description on the generalized Maxwell-Stefan equations. *Chem Eng Sci*. 1990;45:1779–1791.
21. Krishna R, van den Broeke LJP. The Maxwell-Stefan description of mass transport across zeolite membranes. *Chem Eng J*. 1995; 57:155–162.
22. Kapteijn F, van de Graaf JM, Moulijn JA. One-component permeation maximum: diagnostic tool for silicalite-1 membranes. *AIChE J*. 2000;46:1096–1100.
23. van de Graaf JM, Kapteijn F, Moulijn JA. Modeling permeation of binary mixtures through zeolite membranes. *AIChE J*. 1996;45:497–511.
24. Vignes A. Diffusion in binary solutions. *Ind Eng Chem Fund*. 1966;5:189–199.
25. Gardner TQ, Falconer JL, Noble RD, Zieverink MMP. Analysis of transient permeation fluxes into and out of membrane for adsorption measurements. *Chem Eng Sci*. 2003;58:2103–2112.
26. Gardner TQ, Flores AI, Noble RD, Falconer JL. Transient measurements of adsorption and diffusion in H-ZSM-5 membranes. *AIChE J*. 2002;48:1155–1167.
27. Karger J, Ruthven DM. *Diffusion in Zeolites and Other Microporous Solids*. New York: Wiley, 1992:87–122.
28. Yang RT. *Gas Separation by Adsorption Processes*. New York: Butterworths, 1987:49–200.
29. Jee JG, Lee SJ, Lee CH. Three-bed PVSA process for high purity oxygen from ambient air. *AIChE J*. 2005;51:2988–2999.
30. Bakker WJW, Kapteijn F, Poppe J, Moulijn JA. Permeation characteristics of a metal-supported silicalite-1 zeolite membrane. *J Membr Sci*. 1996;117:57–78.
31. Zhen Y, Yong C, Hui L, Gaohong H, Maicun D. Preparation of a novel polysulfone/polyethylene oxide/silicone rubber multilayer composite membrane for hydrogen-nitrogen separation. *Mater Chem Phys*. 2005;94:288–291.
32. Xianshe F, Pinghai S, Robert YMH, Guoliang J, Ren-Xian X. A study of silicone rubber/polysulfone composite membranes: correlating H_2/N_2 and O_2/N_2 permselectivities. *Sep Purif Technol*. 2002;27:211–223.
33. Härtel G, Rompf F, Püschel T. Separation of a CO_2/H_2 gas mixture under high pressure with polyethylene terephthalate membranes. *J Membr Sci*. 1996;113:115–120.
34. David RP, Betty J, Robert CD. Thermal optimization of polybenzimidazole meniscus membranes for the separation of hydrogen, methane, and carbon dioxide. *J Membr Sci*. 2003;218:11–18.

Manuscript received Mar. 19, 2007, and revision received Sept. 15, 2007.